

Article

A Deep Learning-Based Diagnosis System for COVID-19 Detection and Pneumonia Screening Using CT Imaging

Ramzi Mahmoudi ^{1,2,*}, Narjes Benameur ³, Rania Mabrouk ¹, Mazin Abed Mohammed ^{4,*}, Begonya Garcia-Zapirain ^{5,*} and Mohamed Hedi Bedoui ¹

¹ Laboratory of Technologies and Medical Imaging-LTIM-LR12ES06, Faculty of Medicine of Monastir, University of Monastir, Monastir 5019, Tunisia; ranyamab96@gmail.com (R.M.); hedi.bedoui2015@gmail.com (M.H.B.)

² Gaspard-Monge Computer-Science Laboratory, Mixed Unit CNRS-UMLV-ESIEE UMR8049, Paris-Est University, BP99, ESIEE Paris Cité Descartes, 93162 Noisy-le-Grand, France

³ Laboratory of Biophysics and Medical Technologies, Higher Institute of Medical Technologies of Tunis, University of Tunis El Manar, Tunis 1068, Tunisia; narjes.benameur@yahoo.fr

⁴ College of Computer Science and Information Technology, University of Anbar, Ramadi 31001, Iraq

⁵ eVIDA Laboratory, University of Deusto, 48007 Bilbao, Spain

* Correspondence: ramzi.mahmoudi@esiee.fr (R.M.); mazinalshujeary@uoanbar.edu.iq (M.A.M.); mbgarciazapri@deusto.es (B.G.-Z.)



Citation: Mahmoudi, R.; Benameur, N.; Mabrouk, R.; Mohammed, M.A.; Garcia-Zapirain, B.; Bedoui, M.H. A Deep Learning-Based Diagnosis System for COVID-19 Detection and Pneumonia Screening Using CT Imaging. *Appl. Sci.* **2022**, *12*, 4825. <https://doi.org/10.3390/app12104825>

Academic Editors: Huafeng Liu and Jianan Cui

Received: 9 April 2022

Accepted: 6 May 2022

Published: 10 May 2022

Publisher's Note: MDPI stays neutral with regard to jurisdictional claims in published maps and institutional affiliations.



Copyright: © 2022 by the authors. Licensee MDPI, Basel, Switzerland. This article is an open access article distributed under the terms and conditions of the Creative Commons Attribution (CC BY) license (<https://creativecommons.org/licenses/by/4.0/>).

Abstract: **Background:** Severe Acute Respiratory Syndrome Coronavirus 2 (SARS-CoV-2) is a global threat impacting the lives of millions of people worldwide. Automated detection of lung infections from Computed Tomography scans represents an excellent alternative; however, segmenting infected regions from CT slices encounters many challenges. **Objective:** Developing a diagnosis system based on deep learning techniques to detect and quantify COVID-19 infection and pneumonia screening using CT imaging. **Method:** Contrast Limited Adaptive Histogram Equalization pre-processing method was used to remove the noise and intensity in homogeneity. Black slices were also removed to crop only the region of interest containing the lungs. A U-net architecture, based on CNN encoder and CNN decoder approaches, is then introduced for a fast and precise image segmentation to obtain the lung and infection segmentation models. For better estimation of skill on unseen data, a fourfold cross-validation as a resampling procedure has been used. A three-layered CNN architecture, with additional fully connected layers followed by a Softmax layer, was used for classification. Lung and infection volumes have been reconstructed to allow volume ratio computing and obtain infection rate. **Results:** Starting with the 20 CT scan cases, data has been divided into 70% for the training dataset and 30% for the validation dataset. Experimental results demonstrated that the proposed system achieves a dice score of 0.98 and 0.91 for the lung and infection segmentation tasks, respectively, and an accuracy of 0.98 for the classification task. **Conclusions:** The proposed workflow aimed at obtaining good performances for the different system's components, and at the same time, dealing with reduced datasets used for training.

Keywords: SARS-CoV-2; CT scans; deep learning; lung segmentation; infection segmentation; classification; 3D reconstruction

1. Introduction

COVID-19, provoked by the Severe Acute Respiratory Syndrome Corona Virus 2 (SARS-CoV-2), has been spreading exponentially around the world since December 2019 starting from Wuhan, China, resulting in a global health crisis [1]. This highly infectious disease has been posing as the biggest current healthcare threat towards humanity, which has led the World Health Organization (WHO) to declare this outbreak to be a Public Health Emergency of International Concern (PHEIC), and it was recognized as a global pandemic [2,3]. As of 5 April 2021, the WHO reported 131,309,792 worldwide cases with

2,854,276 deaths and a mortality rate exceeding 2% [4]. The typical clinical characteristics of COVID-19 cases range from asymptomatic to flu-like symptoms, fever, dry cough, tiredness, loss of taste and smell, to even a life threatening Acute Respiratory Distress Syndrome (ARDS) [5]. Up to this date, no effective treatment has yet been proven. Hence, accurate and rapid testing is extremely pivotal to lessen the spread of the virus.

The Reverse Transcription-Polymerase Chain Reaction (RT-PCR) test is considered to be the gold standard method for confirming infected cases because it is able to identify SARS-CoV-2 RNA from respiratory specimens, obtained by nasopharyngeal or oropharyngeal swabs, within 4 to 6 h [6]; however, the shortage of RT-PCR test kits is a major problem in many countries around the world. Furthermore, the sensitivity of RT-PCR screening is rather low as a result of high false-negative rates caused by several factors including sample preparation and quality control [7–9]; therefore, chest radiography imaging, X-ray (CXR), or computed tomography (CT scans), is usually used as a complementary examination in the rapid diagnosis and control of the coronavirus. Hence, the use of chest CT scans, as mentioned in this review [10], can counteract the limitations of the low sensitivity of RT-PCR tests, thus improving the accuracy and speed of diagnosis. Moreover, compared with the chest X-ray, CT scans are generally recommended thanks to their three-dimensionality and good visibility. There are various studies inspecting the imaging characteristics throughout the diagnosis, follow-up, and treatment of COVID-19 [11,12]. It was found that patients presented chest radiographic abnormalities which exhibited similar features, including ground-glass opacities (GGO), an area of increased attenuation in the lung with preserved bronchial and vascular markings in the early stages; moreover, they presented pulmonary consolidation when the accumulation of fluid progresses to obscure bronchial and vascular regions in the latter stages. Consequently, accurate and rapid detection and localization of these tissue abnormalities is critical for early diagnosis and treatment of COVID-19.

Recently, with the rapid development of artificial intelligence, and more specifically, deep learning technologies, Convolutional Neural Networks (CNNs) have been used a great deal in medical image processing thanks to their powerful feature representation and extraction. Several techniques based on CNNs have been published, showing promising performances in other disease diagnosing cases, such as cancer and so forth [13,14], which should also have the same achievability in this novel pneumonia detection. In biomedical image analysis, the problems can be interpreted as classification and segmentation to identify and detect abnormal features and regions of interest (ROIs) via deep learning techniques, where the CNN and Unet based architectures are the most promising and popular choice among the research community. In this work, a deep learning-based diagnosis system was developed to automatically detect and analyze areas suspected to be infected with the COVID-19 virus from clinical CT images extracted from a publicly available chest CT scans dataset. Although training accurate and robust models requires sufficient annotated medical imaging data, only one small yet sufficient public dataset is, so far, available because of privacy restrictions and costly labelling. Not to mention that it is likely problematic to combine data sets collected under different labelling regimes, given that generally, the collected data is heavily influenced by the instructions provided to the annotators. For this reason, the proposed framework is aimed at obtaining good performances for the different system's components while dealing with reduced dataset used for training at the same time.

The remainder of this paper is organized as follows. In Section 2, a literature overview is presented. Our proposed method is explained in Section 3. The experimental results are introduced in Section 4, then discussed and compared with recent works in Section 5. Finally, Section 6 concludes the paper, highlights limitations, and proposes future improvements.

2. Related Works

Recently, medical imaging processing techniques have been widely used to monitor several diseases. The progress in this field has been reinforced by the introduction of

Artificial Intelligence technologies that became a popular approach for detection and segmentation of many medical problems thanks to their powerful feature representation [15].

In this context, many approaches have been proposed for the detection and the segmentation of the lungs' COVID-19 infection using chest X-rays and CT scans in the last few months [16], which confirmed that a carefully designed image examination procedure plays a vital role in reducing the diagnostic burden. The proposed methods can be classified into three categories: (1) classification techniques; (2) infected regions and segmentation techniques and; (3) diagnosis systems that worked on both tasks. Table 1 presents two proposed methods for each category as well as the deep learning architectures used in each one of them and the images' modality they used.

Table 1. A summary of the recently published studies on COVID-19 detection approaches.

	Method	Images' Modality	Approach
Classification	Wang et al. COVID-Net [17]	X-ray	A deep residual CNN based model
	El Araby et al. GSEN architecture [18]	X-ray	A novel Gray-Scale spatial exploitation learning Net (GSEN) for COVID-19
	Ahuja et al. Deep transfer learning [19]	CT-scans	ResNet18 pre-trained transfer learning-based model
Infection Segmentation	Fan et al. Inf-Net [20]	CT-scans	DL approach based on three reverse attention modules connected to a paralleled partial decoder
	Shan et al. VB-Net [21]	CT-scans	A modified 3D CNN that combines V-Net with the bottle-neck structure
	Elzeki et al. (CNN-VGG19) [22]	X-ray	DL approach based on fusion algorithm using NSCT with deep learning VGG19
Diagnosis System	Wu et al. JCS [23]	CT-scans	Classification: Res2Net; Infection segmentation: VGG16 backbone + Enhanced Feature Module + Attentive Feature Fusion
	Gozes et al. [24]	CT-scans	Classification: Resnet-50—2D deep CNN; ROI extraction: Unet; Infection detection: Grad-cam technique and a commercial off-the-shelf software for lung pathology detection

Wang et al. [17] introduced COVID-Net, a densely-connected deep convolutional neural network design, tailored for the detection of COVID-19 cases from chest X-ray images, and it achieved a 93.3% test accuracy. A three-phase detection model using deep transfer learning is proposed, in the work of Ahuja et al. [19] to improve the detection accuracy, and it was proven that the ResNet18 architecture helped to attain a better classification accuracy (99.4%) compared with the other considered architectures. Fan et al. [20] developed a new Deep Network called "Inf-Net" to automatically identify infected regions from chest CT slices. The algorithm is based on a parallel partial decoder able to aggregate the high-level features and to generate a global map. In their study, they used a small dataset of 100 CT labeled images which achieved a dice score of 0.682. A semi-supervised segmentation system was then introduced to alleviate the shortage of labeled data and it achieved a dice score of 0.739. Similarly, Shan et al. [21] proposed a deep learning based system for automatic segmentation and quantification of infection regions from chest CT scans. A modified 3D CNN that combines V-Net [25] with the bottle-neck structure was used and they achieved a Dice coefficient of 91.6%. Another study developed by Elzeki et al. [22] who proposed a novel approach that combines CNN and VGG19 to detect COVID-19 features in chest X-ray images. In their study, they used a dataset of eighty-seven chest X-ray images associated with twenty-five cases and they obtained an accuracy of 96.93%, a sensitivity of 57.14%, and a specificity of 99.2%. A joint classification and segmentation system was proposed by Wu et al. [23] for a real-time diagnosis of COVID-19. The classification model is a Res2Net-based [26] classifier that achieved an average sensitivity of 95.0% and a specificity of 93.0%. The segmentation model is based on an encoder, with VGG-16 backbone [27] added with an Enhanced Feature Module, and a decoder based on Attentive Feature Fusion strategy. The model succeeded to segment the infected regions with a dice score of 78.3.

Gozes et al. [24] presented a system that detects cases suspected to have COVID-19 features from CT images, using a Resnet-50—2D deep CNN architecture [28] with 94% sensitivity and 98% specificity; then, for cases classified as positive, an abnormality localization module will be executed to extract, using a Grad-cam technique [29], the network's activation maps that contributed most to the decision. An infection analysis will be further held using commercial off-the-shelf software to detect nodules and small opacities to reinforce the infection localization.

3. Method

In this section, our proposed approach is presented in detail. We start with demonstrating the architecture design methodology behind the proposed approach. We then describe the data set used for training our models and provide details of the proposed network architectures, along with their different components, and we point out the training strategy along with some implementation details. At the end, we display the real runtime workflow of our proposed diagnosis system.

3.1. CNN and U-Net

Convolutional Neural Networks (CNN) [30,31] are a powerful tool which has already demonstrated their success in classification tasks, where the output of an image is a single class label. For almost any computer vision problems, CNN-based approaches surmount other techniques, and it may even surpass human experts in the corresponding domain.

However, in several visual tasks, particularly in biomedical image processing where reliable image segmentation is one of its crucial tasks because it demands us not only to determine whether there is a disease, but also to delimit the abnormal regions, the desired output ought to cover localization, meaning that a class label is supposed to be attributed to each pixel. Over the last few years, different methods that improved traditional deep learning approaches have been developed in order to address the problem of creating CNNs producing a segmentation map for a whole input image in a sole forward pass [32,33].

One of the most acknowledged state of the art deep learning methods is the Fully Convolutional Network [34]. Its key point is to use the CNN as an effective feature extractor. It consists of replacing the fully connected layers with convolutional ones to output spatial feature maps, which are further up-sampled to produce dense pixel-wise output, instead of classification scores.

The FCN's topology consists of two parts: a down-sampling path in charge of capturing semantic information and an up-sampling path in charge of recovering spatial information. A skip connection operation is used for mitigating information loss as a result of pooling or down-sampling layers. The U-Net neural is another popular biomedical segmentation model, originally proposed by Ronneberger et al. for biomedical image processing, and the winner of the ISBI cell tracking challenge in 2015 by a large margin [35]. This architecture has so far proved itself in binary image segmentation competitions such as satellite image analysis [36], medical image analysis [13], and others [37].

The encoder part is responsible for capturing context following the typical architecture of a CNN with alternating convolution and pooling operations. It is composed of five blocks, which are each composed of two convolutional layers, using a ReLU (Rectified Linear Unit) activation function that provides nonlinearity to the network; they produce feature maps through a convolution process; one max-pooling layer down-samples those feature maps, hence, reducing their size, and increasing their number per layer at the same time, so that the architecture can effectively learn the complex structures.

The decoder part is responsible for decoding the information, thus enabling precise localization, by using transposed convolution (deconvolution) operations to finally produce the segmentation mask of the image. It is also made of five blocks, each composed of two convolutional layers, which also utilizes the ReLU as the activation function; one up-sampling layer which is responsible for restoring the feature maps to their original size in

the network by reverting the max-pooling operation; and a skip connection that combines the up-sampled features with high-resolution encoded features from the encoder part.

The general architecture of a U-Net model is illustrated in Figure 1. It is made up of two major sections, namely, the encoder and decoder.

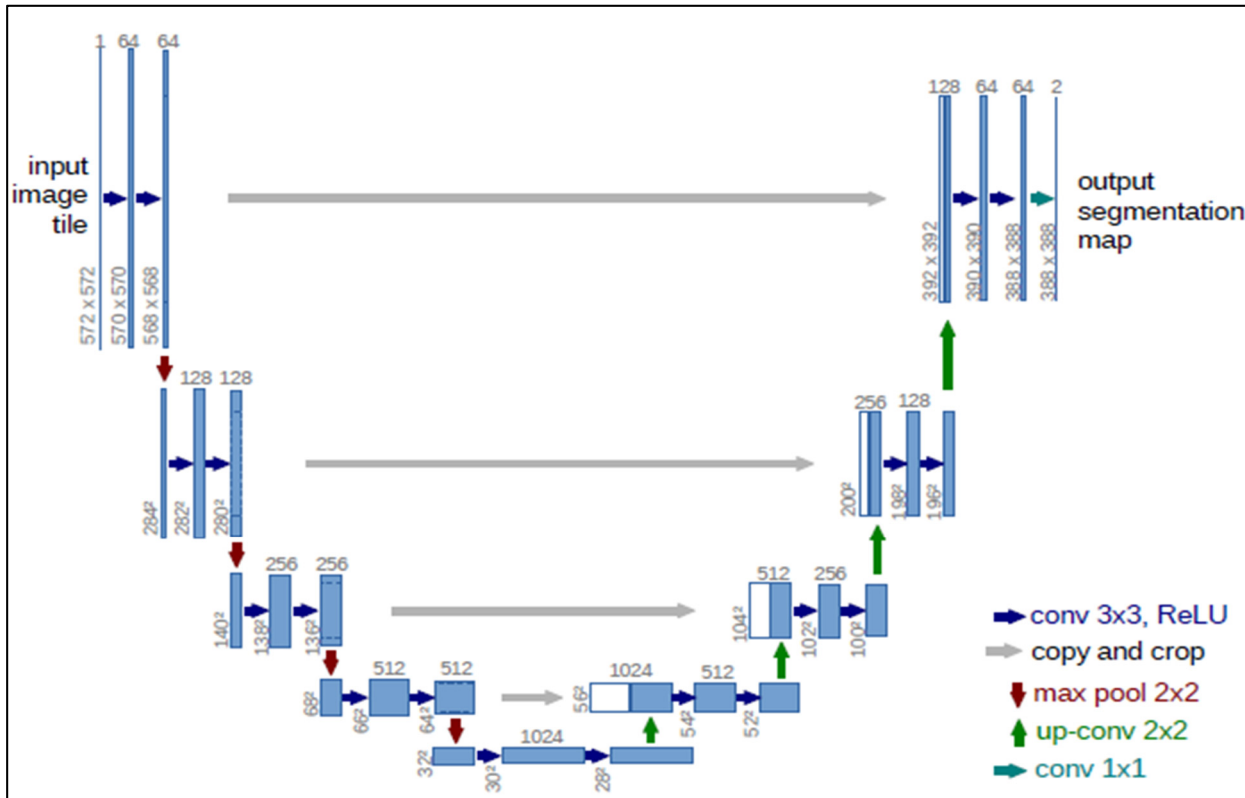


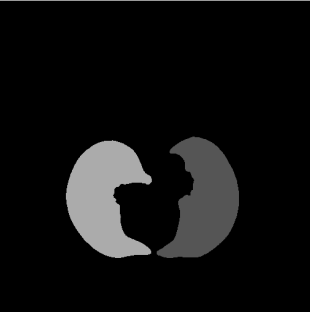
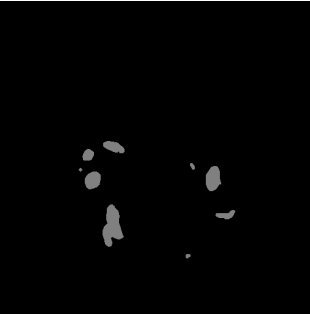
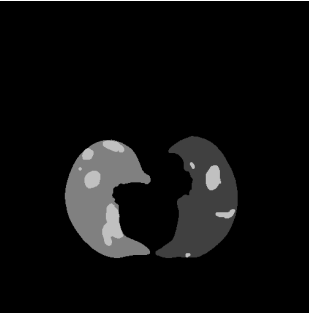
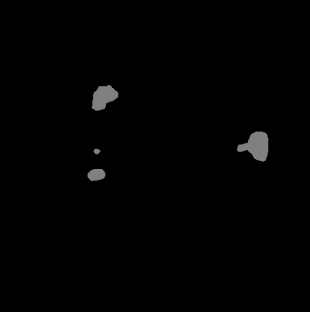
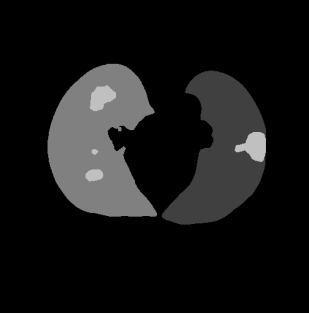
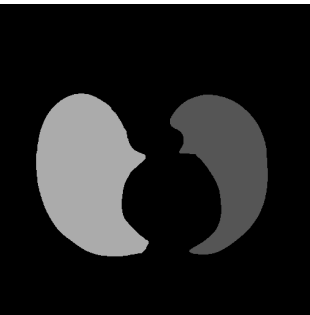
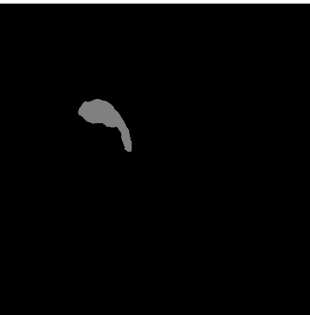
Figure 1. U-net architecture [32].

3.2. Dataset

In spite of the growing number of COVID-19 infected patients, along with their volumetric CT scans, labeled CT scans are still only available in a limited capacity. Hence, publicly accessible CTS datasets are very limited. For this reason, we chose to use the lung CTS dataset of Ma Jun et al. [38] to train and evaluate our proposed network which is, to the best of our knowledge, the first publicly available data-efficient learning benchmark for medical image segmentation.

The dataset was collected from the Corona-cases Initiative [39] and Radiopaedia [40], and was manually annotated in the work of Ma Jun et al. [41]. It is composed of twenty axial volumetric CT scans related to confirmed COVID-19 subjects and it is composed of a total of 3.138 lung CT images, labeled, segmented, and verified by expert radiologists, along with their correspondent lung CT images, their corresponding lung masks, infection masks, and a superposition of the two masks, respectively. Table 2 gives an overview of the used database.

Table 2. Three sample images from the used dataset. First column: original CT scans. Second column: lung masks. Third column: infection masks. Fourth column: superposition of the lung and infection masks.

Original CT Scan	Lung Mask	Infection Mask	Lung and Infection Masks
			
			
			

3.3. Network Architecture

In this section our proposed approach is provided and described in Figure 2. As the figure shows, the architecture consists of four main processes. Starting with the 20 CT scan cases, we portioned the data to be 70% for the training dataset and 30% for the validation dataset. First, we started with the lung segmentation phase. We used the Contrast Limited Adaptive Histogram Equalization preprocessing method to remove noise and intensity inhomogeneity. Then, we removed all the black slices to only crop the region of interest containing the lungs.

A Unet architecture, based on CNN encoder and CNN decoder approaches, is then introduced for fast and precise image segmentation to obtain the lung segmentation model. We then proceeded the exact same way to obtain the infection segmentation model in the second phase, and to further improve the model and to better estimate its skill on unseen data, we used fourfold cross-validation as a resampling procedure for the evaluation.

In the third phase, we augmented the data which was then fed to our proposed three layer CNN architecture, with additional fully connected layers, followed by a Softmax layer for the COVID-19 classification. The last phase is the volume reconstruction of the twenty cases. We reconstructed the lungs' volumes first, then the infection volumes for each

case, in order to calculate the volume ratio to obtain, at last, the corresponding infection rates. A detailed description of the four processes' components will be described in the later sections.

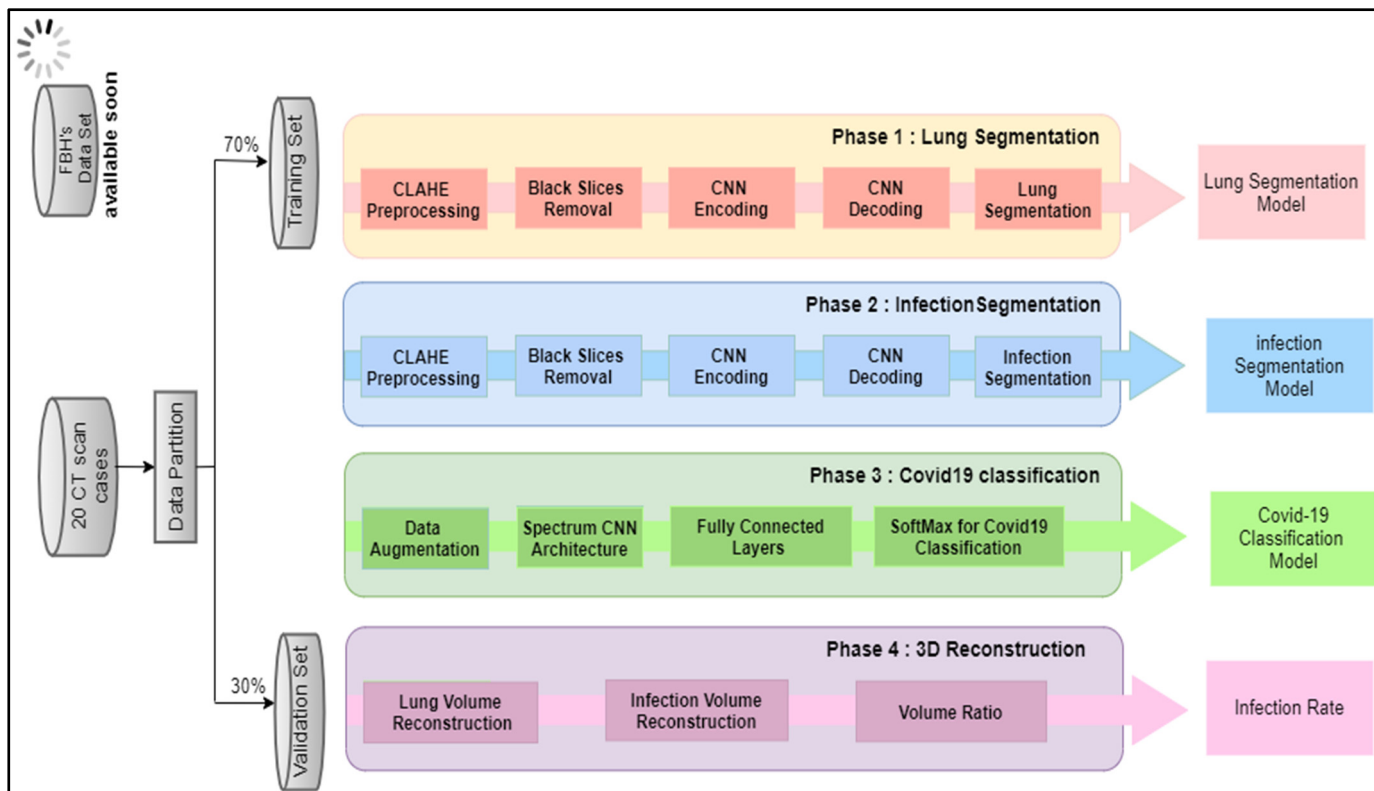


Figure 2. Flowchart of the different phases involved in the proposed diagnosis system.

3.4. Data Preprocessing

Since medical images suffer a lot from contrast problems such as noise and intensity inhomogeneity, the Contrast Limited Adaptive Histogram Equalization (CLAHE) method, proposed in [42], was used to enhance the contrast of the obtained images. It is a variant of adaptive histogram equalization (AHE), and its main idea is to find the mapping for each pixel based on its local (neighborhood) grayscale distribution using a transformation function that limits the contrast amplification in highly concentrated regions. In fact, the CLAHE demonstrated good results on medical images, and has shown its effectiveness in assigning displayed intensity levels in chest CT scans in particular [43,44].

Furthermore, the CT scans contain a lot of black slices and parts which we are not interested in, such as the diaphragm below the lungs, which takes up valuable RAM and unnecessary computing in the network. For this reason, we chose to crop only the region of interest (ROI) that contains the lungs: the contour (largest closed boundary) with the largest area would be the contour covering the lungs. We concatenated the 2nd and 3rd largest contours for the two lungs individually in order to get the maximum ROI in the same resolution. In addition, when cropping a CT scan, we made sure that its corresponding segmentation map is also cropped by the same limits, otherwise pixel level labeling will go wrong. Below, Figure 3 illustrates the impact of applying the CLAHE filter on an input chest CT scan.

The Figures 4 and 5 below illustrate a chest CT scan and its corresponding lung and infection mask, respectively, before and after cropping and applying the CLAHE filter. The impact of the filter on the sharpness of the image is clearly identifiable.

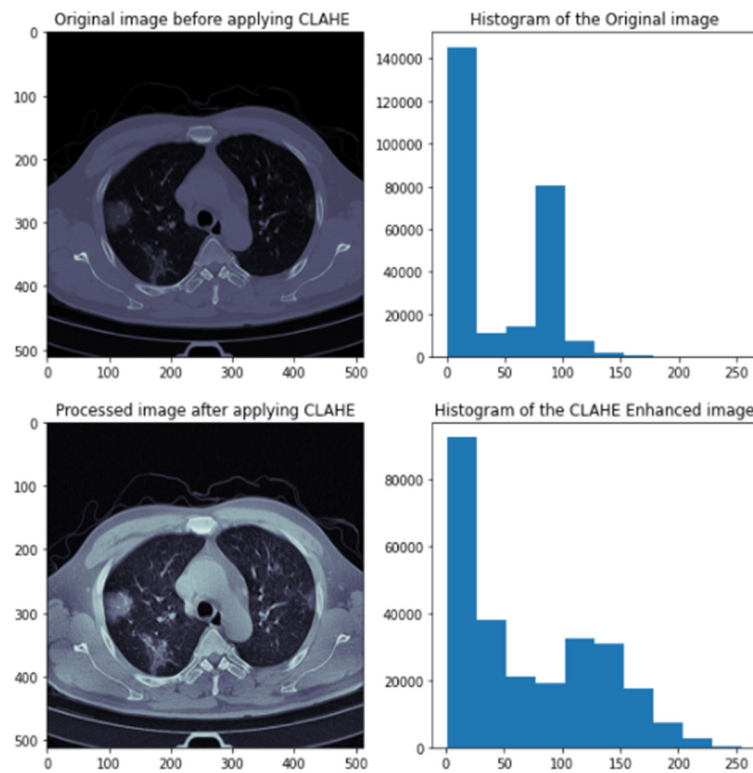


Figure 3. The impact of applying the CLAHE filter on an input chest CT scan.

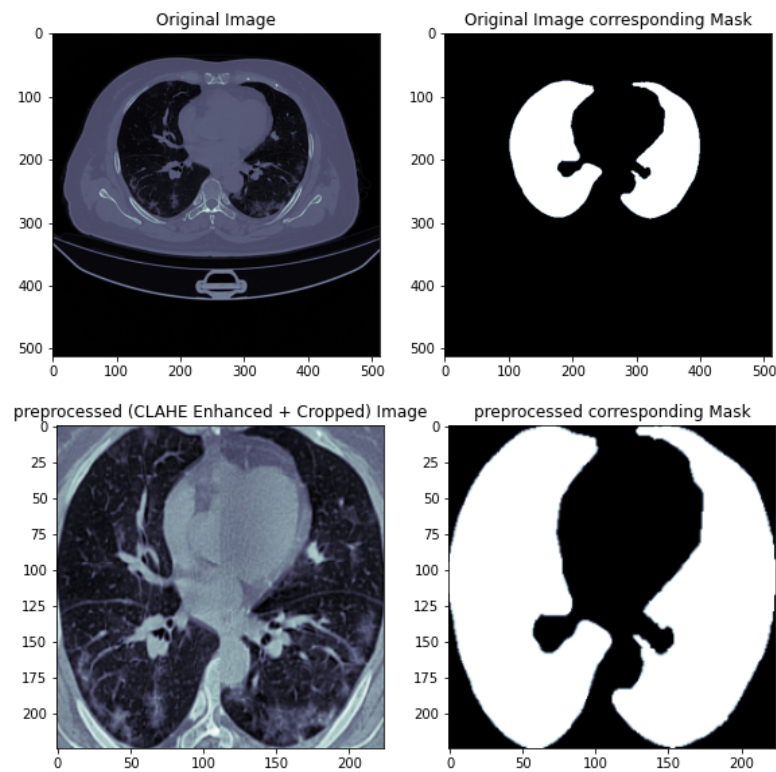


Figure 4. A chest CT scan and its corresponding lung mask before and after cropping.

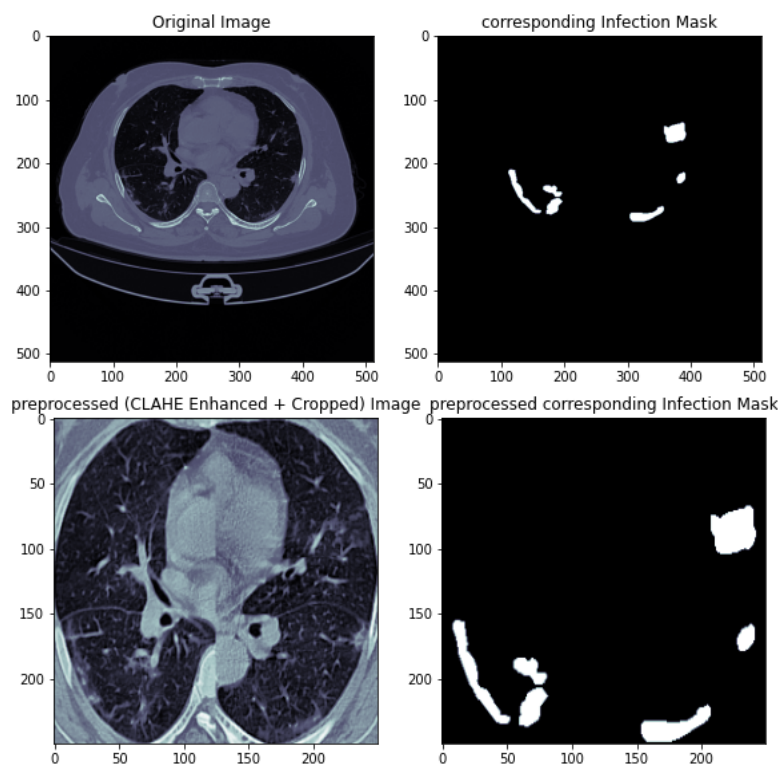


Figure 5. A chest CT scan and its corresponding infection mask before and after cropping.

3.5. Data Augmentation

In order to overcome the limited size of the dataset size and to avoid the overfitting problem, we augmented our data by randomly applying typical transformation techniques [45] including rotations, horizontal and vertical translations and flips, shearing and scaling.

3.6. Models Description

3.6.1. Segmentation Models

The proposed network includes the segmentation of lung and COVID-19 infection segmentation. Both models were trained separately. The standard U-Net was implemented using the keras library with the tensorflow backend, consisting of five blocks encoding path and a symmetric five blocks decoding path. At each level of the encoder, a convolution operation, a ReLU activation function, and a batch normalization operation were applied two times consecutively, followed by a max-pooling operation, to overcome the overfitting issue by minimizing the spatial size of the convolved features, before moving to the next level. The decoder recovers the original input size by applying the same sequence of operations by replacing the max-pooling operation with the transposed convolution as an up-sampling operation at every level. Additionally, the corresponding feature from the encoder is concatenated to the decoder's block input. A 1×1 convolution, with a sigmoid activation function, was then finally added for the generation of the final binary prediction map. The network used thirty-two feature maps at its highest resolution and 512 at its lowest. The convolutions were applied with a kernel size of 3×3 , and the transposed convolutions were applied with a kernel size of 2×2 with a stride of 2×2 . The network was trained, and the parameters were updated using the Adam optimizer with 0.0005 as a learning rate. To further optimize the training procedure, we used the cosine annealing scheduler, implemented as a custom callback, where learning rate starts at 0.0005 and then is dropped rapidly to 0.0001 before being increased again to the maximum. Both networks were trained with a batch size of thirty-two, and 80 and 16 epochs for lung and infection segmentations, respectively.

3.6.2. Classification Models

For the classification task we implemented three layers CNN where each layer was composed of two convolution operations, each followed by a batch normalization operation, and a max-pooling operation. A dense layer, using the ReLU activation function with a dropout of 0.4, was then introduced followed by the last dense layer for classification using the Softmax activation function and the binary cross entropy loss function. The network used sixteen feature maps at its highest resolution and sixty-four at its lowest. The convolutions were applied with a kernel size of 3×3 . The network was trained with thirty-two batch size and twenty-five epochs, and the parameters were updated using the Adam optimizer with 0.0005 as a learning rate.

3.7. Volume Reconstruction

The last phase is the volume reconstruction of studied cases. We reconstructed the lungs' volumes at first then the infection volumes in order to calculate the volume ratio of each case to obtain at last the correspondent infection rate. For this step, we used the platform Thermo Scientific Amira Software [46], which is a powerful multifaceted 2D–5D platform for visualizing, manipulating and understanding data from many image modalities including CT, MRI, and others. Below, Table 3 demonstrates the volume ratios calculated using the lung and infection reconstructed volumes of the 20 patients from the used dataset which respects the fact that the proportion of infections in the lungs range from 0.01% to 59% as stated in [41].

Table 3. Quantitative results of the volume reconstruction phase for three different patients from the used dataset.

	Slices Number	Lungs Volume	Infection Volume	Volume Ratio	Infection Severity
P1	301	3312776	408920	0.1234	Moderate
P2	200	4622672	181422	0.0392	Mild
P3	200	3498208	1015819	0.2903	Severe
P4	270	4536387	59529.4	0.0131	Mild
P5	290	4746608	80654.7	0.0169	Mild
P6	213	4430680	125977	0.0284	Moderate
P7	249	2916567	88225.8	0.0302	Moderate
P8	301	3818469	278690	0.0729	Moderate
P9	256	2639075	101621	0.0385	Moderate
P10	301	2274445	396574	0.1743	Severe
P11	39	5516346	1067853	0.1935	Severe
P12	45	5736035	1044140	0.1820	Severe
P13	39	4617109	156231	0.0338	Moderate
P14	418	8186436	263209	0.0321	Moderate
P15	110	4138735	1023851	0.2473	Severe
P16	66	7882785	777185	0.0985	Moderate
P17	42	3136991	9.01817	0.003	Mild
P18	45	5729041	46320.6	0.0080	Mild
P19	45	6664643	148246	0.0222	Mild
P20	93	4842892	2844976	0.5874	Severe

As the table shows, the used dataset contains a total of six mild infected patients having a volume ratio inferior to 0.02, eight moderately infected patients having a volume ratio between 0.02 and 0.15 and six severely infected patients having a volume ratio superior to 0.15. This clearly demonstrates that we used a well-balanced dataset. Figure 6a–c below illustrate the volume reconstruction of the lungs and its corresponding infection regions of the most representative three patients, respectively. Volume reconstruction for all patients is given in Figure 7.

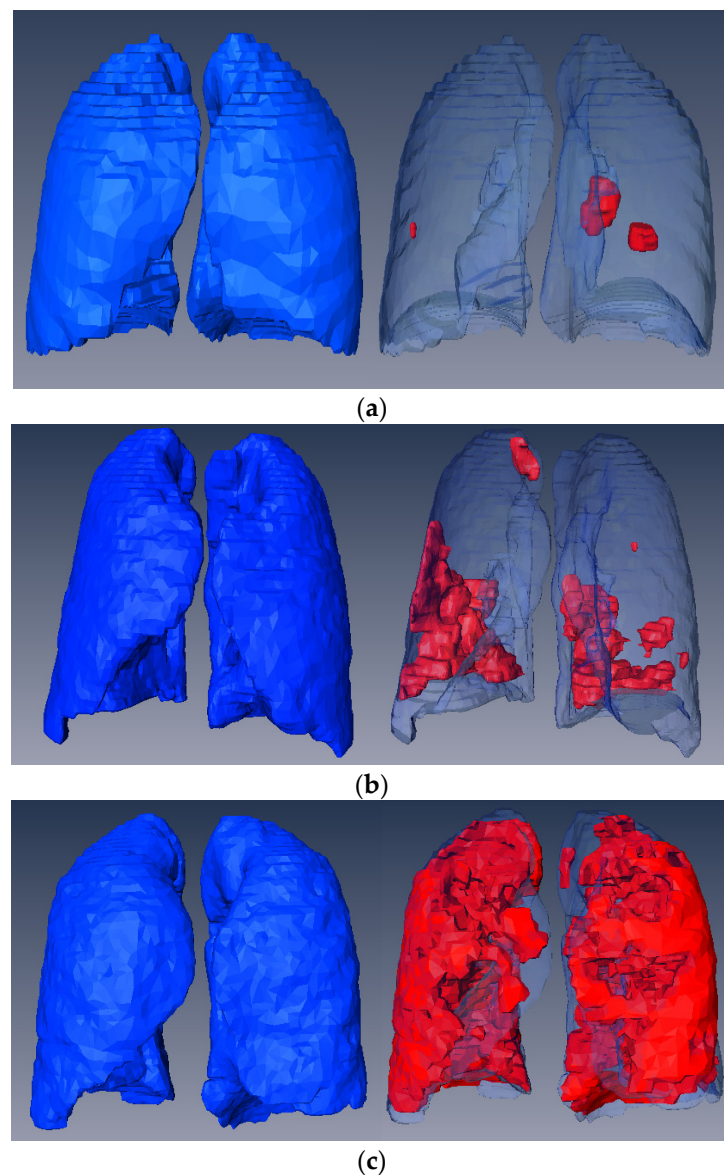


Figure 6. Volume reconstruction of the lungs and its correspondent infection regions of: (a) a patient presenting a mild infection; (b) a patient presenting a moderate infection; (c) a patient presenting a severe infection.

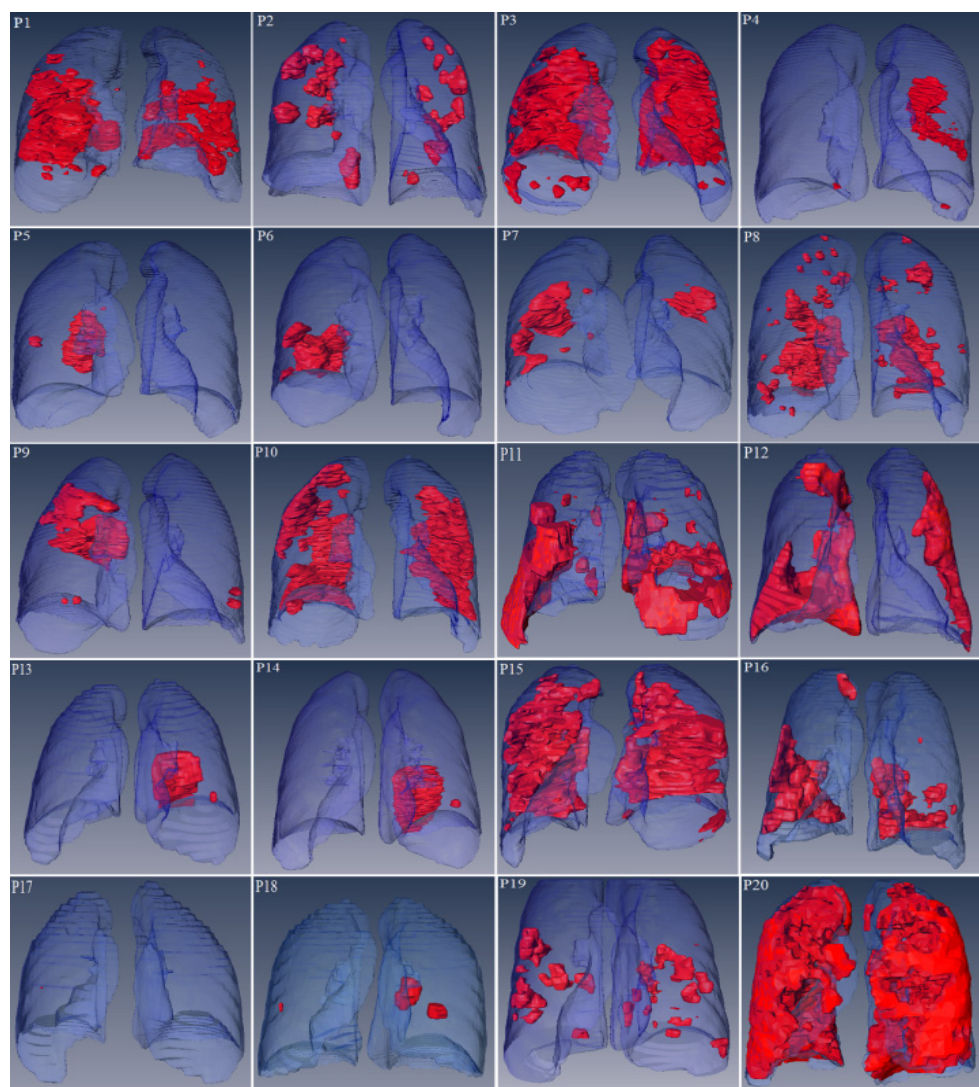


Figure 7. Volume reconstruction of the lungs and its corresponding infection regions of the twenty patients.

3.8. Real Runtime Flowchart

Below, Figure 8 presents the real run time flowchart of our proposed system. For input CT scan slices, the lung segmentation model will first be executed to output the lung masks that will be used for the region of interest extraction by superposing them with the input slices. Then, as the user chose, either the classification model will be executed in case of a rapid diagnosis choice, or the infection segmentation model will be executed in case of a full diagnosis choice. In the first case, the classification model will be executed, using the extracted ROIs, to verify whether the patient is infected or not. In the latter case, the infection segmentation model will be executed, using the extracted ROIs, to obtain the infection masks. The lung and infection volume construction will then be held for the calculation of the infection rate by calculating the volumes' ratios that will give us, at last, an idea about the infection severity.

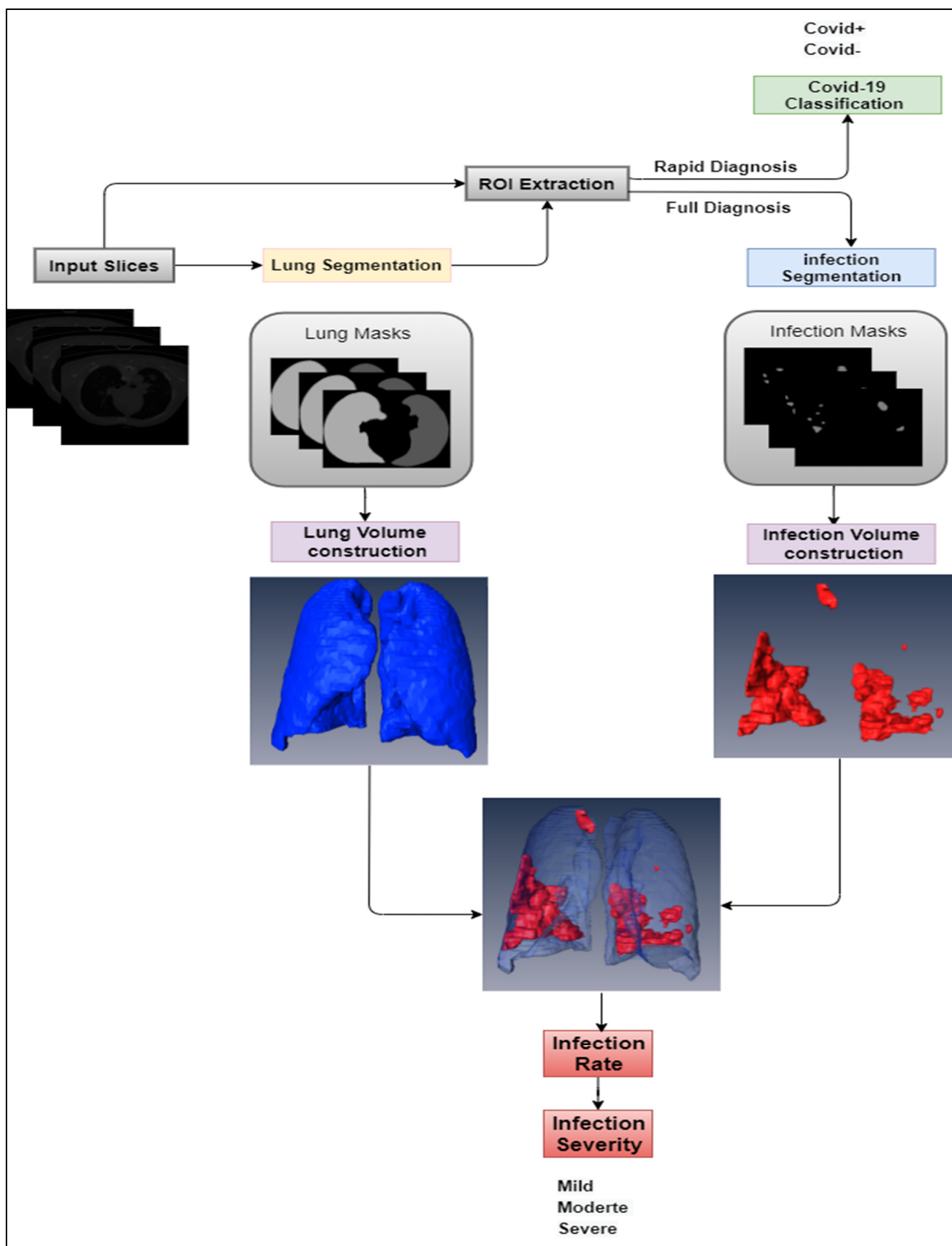


Figure 8. Real Runtime flowchart.

4. Experimental Results

In this section, we demonstrate the aptness of our proposed method by providing a detailed experimental analysis presenting both quantitative and qualitative results as well as comparing our results with other state of the art methods.

4.1. Evaluation Metrics

There are several metrics that are used by the research community for medical image analysis to measure the performance of classification and segmentation models, including precision, recall, dice coefficient and intersection over union (IoU). To calculate these metrics, the following four measures are required:

True Positive (TP): represents the number of pixels being correctly identified in the segmentation tasks and the number of correctly predicted infected CTs in the classification task.

True Negative (TN): denotes the number of non-lung/infection pixels being correctly identified as non-lung infection in the segmentation tasks and the number of correctly predicted healthy CTs in the classification task.

False Positive (FP): represents the number of non-lung/infection pixels being wrongly classified as lung/infection pixels in the segmentation tasks and the number of mistakenly predicted infected CTs in the classification task.

False Negative (FN): denotes the lung/infection pixels being wrongly classified as non-lung/infection pixels in the segmentation tasks and the number of mistakenly predicted healthy CTs in the classification task.

Accuracy: this metric measures the ratio of correctly identified predictions divided by the entire predictions and it is defined in Equation (1).

$$\text{Accuracy} = \frac{\text{TP} + \text{TN}}{\text{TP} + \text{TN} + \text{FP} + \text{FN}} \quad (1)$$

Precision: this metric is a measure of exactness calculated as the ratio of true positive predictions divided by the number of predicted positives and defined in Equation (2).

$$\text{Precision} = \frac{\text{TP}}{\text{TP} + \text{FP}} \quad (2)$$

Recall: this metric is a measure of completeness calculated as the ratio of true positive predictions divided by the number of actual positives and defined in Equation (3).

$$\text{Recall} = \frac{\text{TP}}{\text{TP} + \text{FN}} \quad (3)$$

Area Under the Receiver Operating Characteristic Curve (AUROC): this metric is a measure of separability that summarizes the ROC curve which plots the rate of true positive predictions versus the false positive ones for all possible thresholds.

Area Under the Precision Recall Curve (AUPRC): this metric is another measure of separability that summarizes the PR curve which plots the precision versus the recall for all thresholds.

Dice Coefficient (also known as Dice score): it is the overlap ratio between the prediction and the ground truth, giving more weight to the intersection between the two. Its value ranges between 0 and 1, and the higher the value is, the better the segmentation result. It is defined in Equation (4) as follows:

$$\text{Dice} = \frac{2\text{TP}}{2\text{TP} + \text{FP} + \text{FN}} \quad (4)$$

Intersection over Union IoU (also known as Jaccard index/F1 score): it is another popular metric that measures the overlap between the prediction and the ground truth and is defined in Equation (5).

$$\text{IoU} = \frac{\text{TP}}{\text{TP} + \text{FP} + \text{FN}} \quad (5)$$

4.2. Quantitative Evaluation

4.2.1. Learning Phase

We start by studying the learning phase. Figure 9 demonstrates the Dice Coefficient and the Dice Loss Training curves of the lung's segmentation model, respectively.

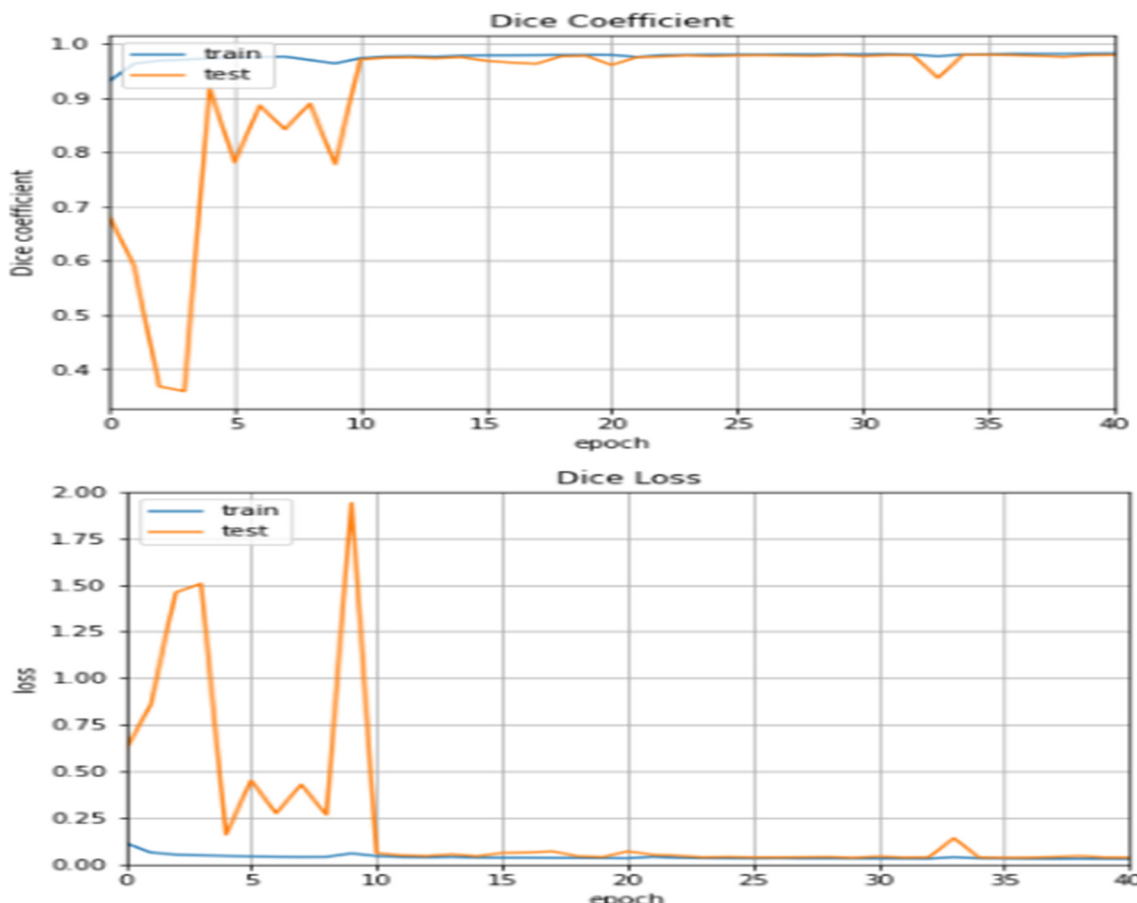


Figure 9. Dice Coefficient and Dice Loss Training curves of the lung's segmentation model.

As the figure shows, the plots of training and validation loss decreased to a point of stability which confirms the good performance of the proposed model on unseen data. Figure 10 demonstrates the Dice Coefficient and the Dice Loss Training curves of the infection segmentation model respectively for the different folds.

The curves clearly confirm the good performance of the proposed model on unseen data in the different folds, as the training and validation loss decreased to a point of stability. Figure 11 demonstrates the Loss Training curve of the classification model.

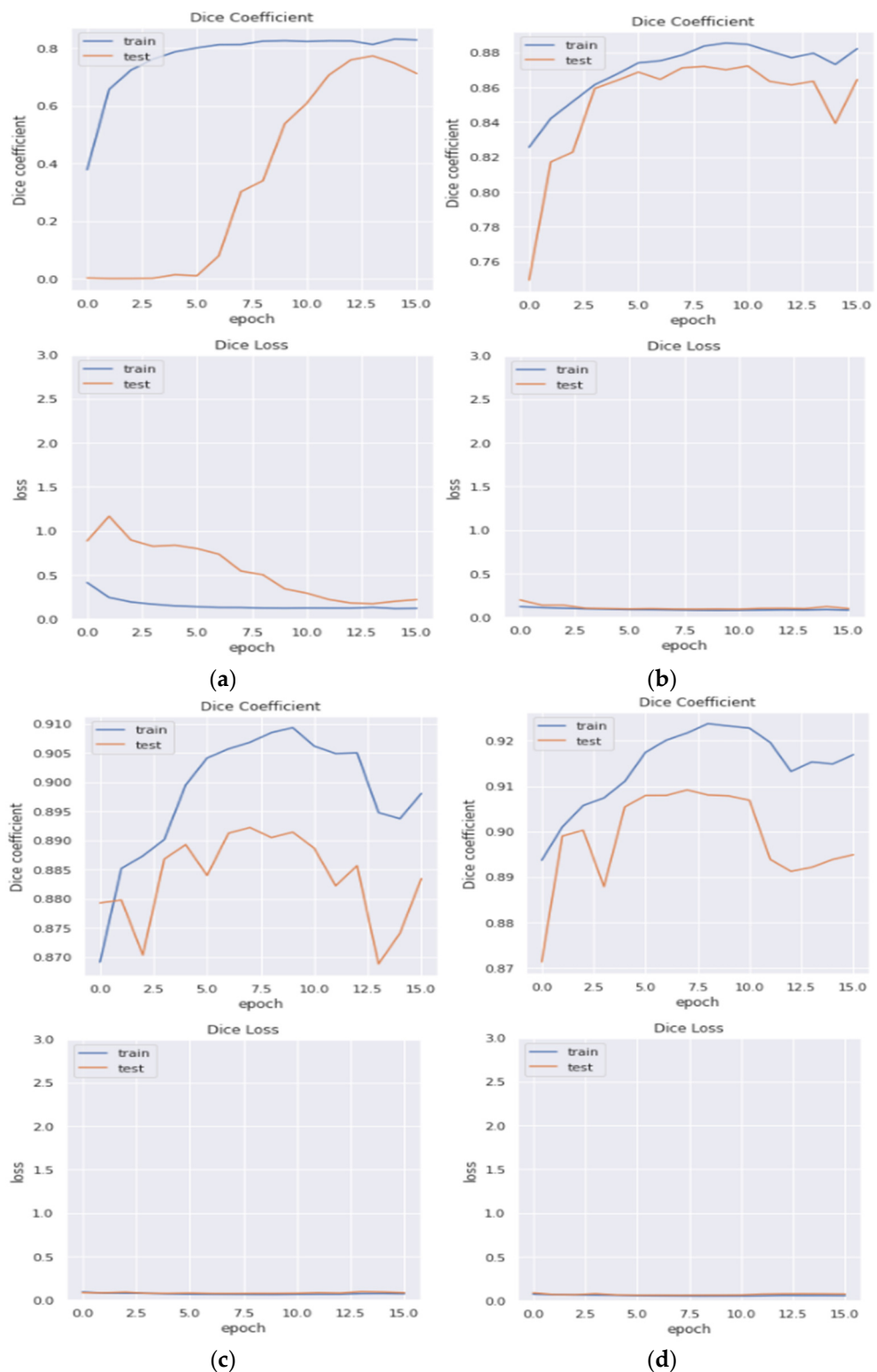


Figure 10. (a) Dice Coefficient and Dice Loss Training curves of the infection segmentation model using fold 1. (b) Dice Coefficient and Dice Loss Training curves of the infection segmentation model using fold 2. (c) Dice Coefficient and Dice Loss Training curves of the infection segmentation model using fold 3. (d) Dice Coefficient and Dice Loss Training curves of the infection segmentation model using fold 4.

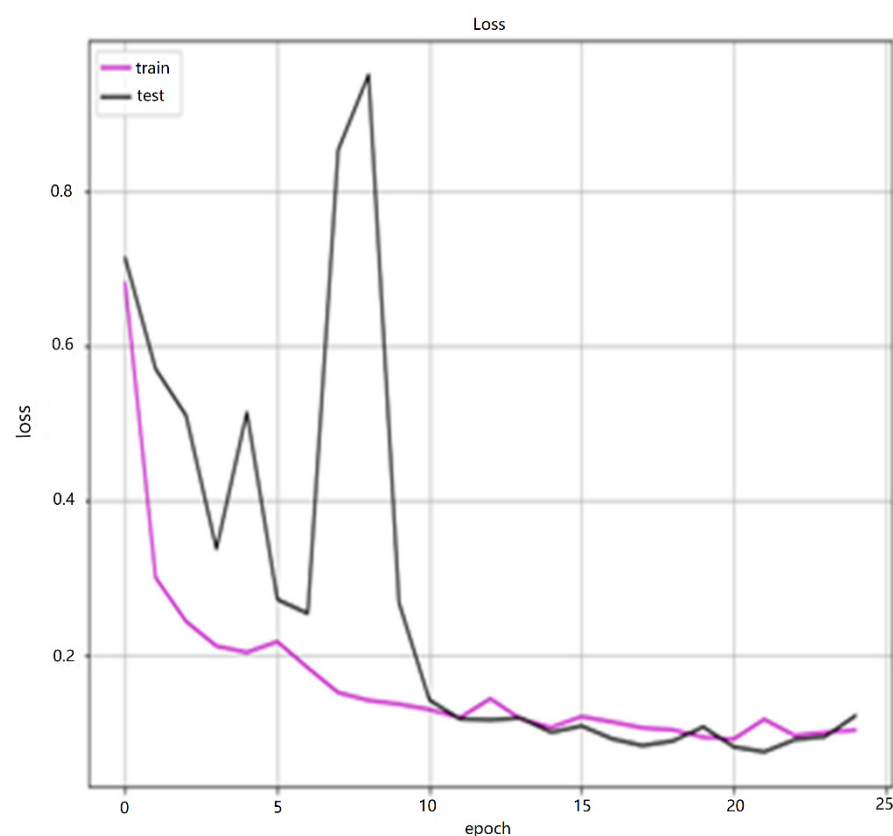


Figure 11. Classification model's loss curve.

4.2.2. Validation Phase

The quantitative evaluation demonstrated the good performance of our proposed system as justified by the reached values of the evaluation metrics for the three tasks in Table 4 below. The attained dice coefficient values are 0.98 for the lung segmentation model and 0.91 for infection segmentation model. Additionally, we achieved an accuracy of 0.95, 0.94, and 0.98 for lung segmentation, infection segmentation, and classification models, respectively.

Table 4. Quantitative results among different tasks on testing set in terms of accuracy and Dice Coefficient values.

Task	Accuracy	Dice Coefficient
Lung Segmentation	0.95	0.98
Infection Segmentation	0.94	0.91
COVID-19 Classification	0.98	-

Figure 12 below displays fourfold obtained dice for different chosen thresholds.

	1	2	3	4
0.30	0.926285	0.927737	0.924545	0.902083
0.35	0.926417	0.927945	0.924549	0.902039
0.40	0.926351	0.927999	0.924454	0.901944
0.45	0.926100	0.927844	0.924179	0.901761
0.50	0.925787	0.927601	0.923860	0.901416
0.55	0.925327	0.927345	0.923362	0.901056
0.60	0.924798	0.926896	0.922741	0.900536
0.65	0.923978	0.926253	0.921864	0.899834
0.70	0.923070	0.925389	0.920770	0.899008
0.75	0.921664	0.924338	0.919334	0.897817

Figure 12. Fourfold obtained dice for different chosen thresholds.

As the figure shows, the maximum validation dice was on the second split as the value reached 0.927999. Hence, we consider that the best threshold to be used later for the calculation of the other metrics is 0.40. The mean of all obtained dice is 0.9189. The results of the fourfold cross-validation for the different metrics are summarized in Table 5.

The model achieved a dice coefficient of 0.91, an IoU of 0.85, a precision 0.92, a recall of 0.90, an AUROC of 0.95, and an AUPRC of 0.91. The high AUROC and AUPRC values demonstrate that our model succeeded in handling and distinguishing both infected regions and non-infected ones well.

Table 5. Fourfold cross-validation results of the Infection segmentation model calculated as the mean of folds.

Dice Coefficient	IoU	Precision	Recall	AUROC	AUPRC
0.91	0.85	0.92	0.90	0.95	0.91

4.3. Qualitative Evaluation

The qualitative evaluation proved that our predicted masks are notably close to the ground-truth masks, as shown in Figures 13 and 14 below, which display four sample images from the test set for the lung segmentation task and infection segmentation task, respectively.

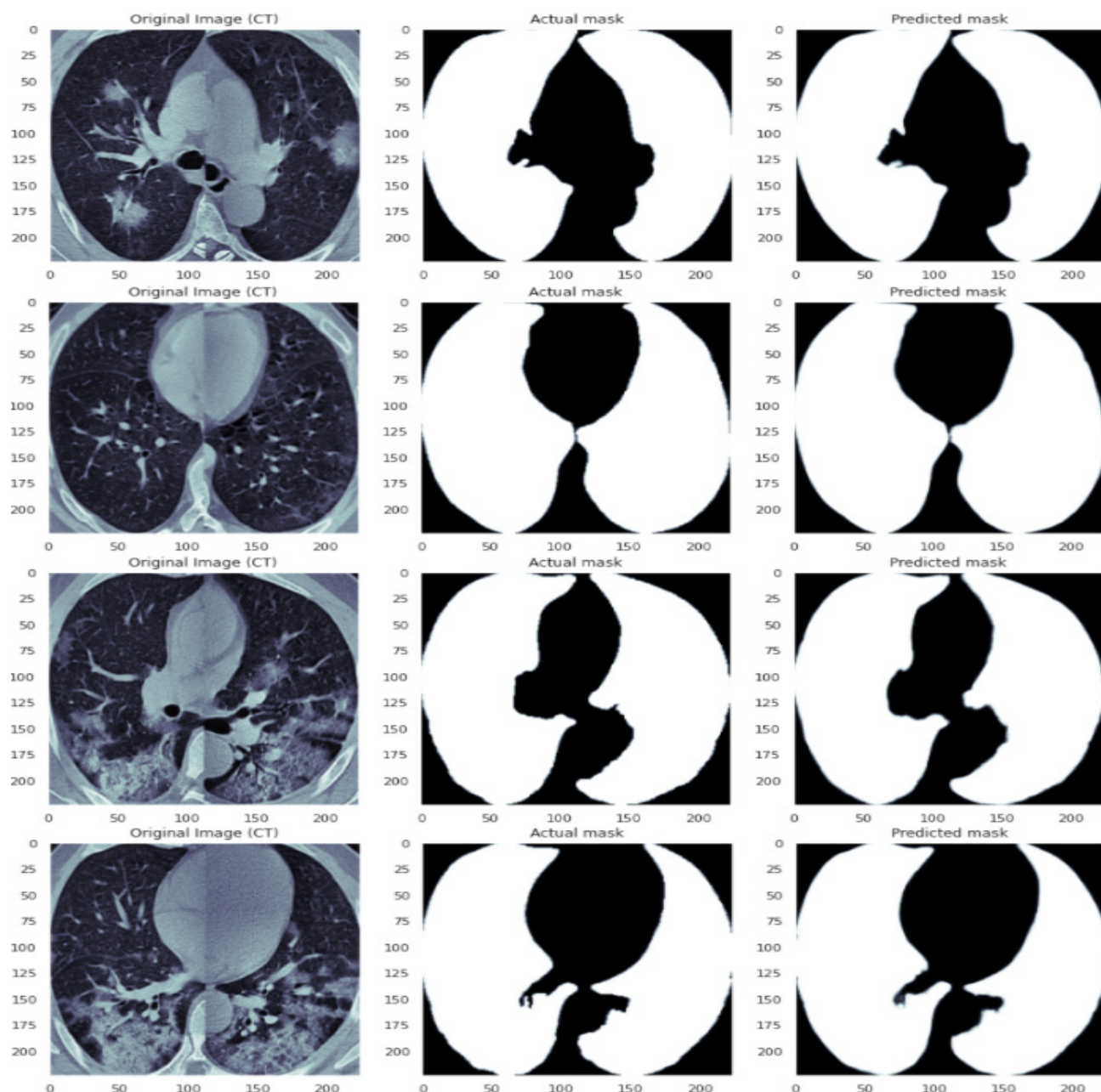


Figure 13. Visual qualitative comparison of the lungs segmentation results between the ground truth and our proposed model on four slices from different CT scans. First column: original CT scan. Second column: ground truth. Third column: predicted lung masks.

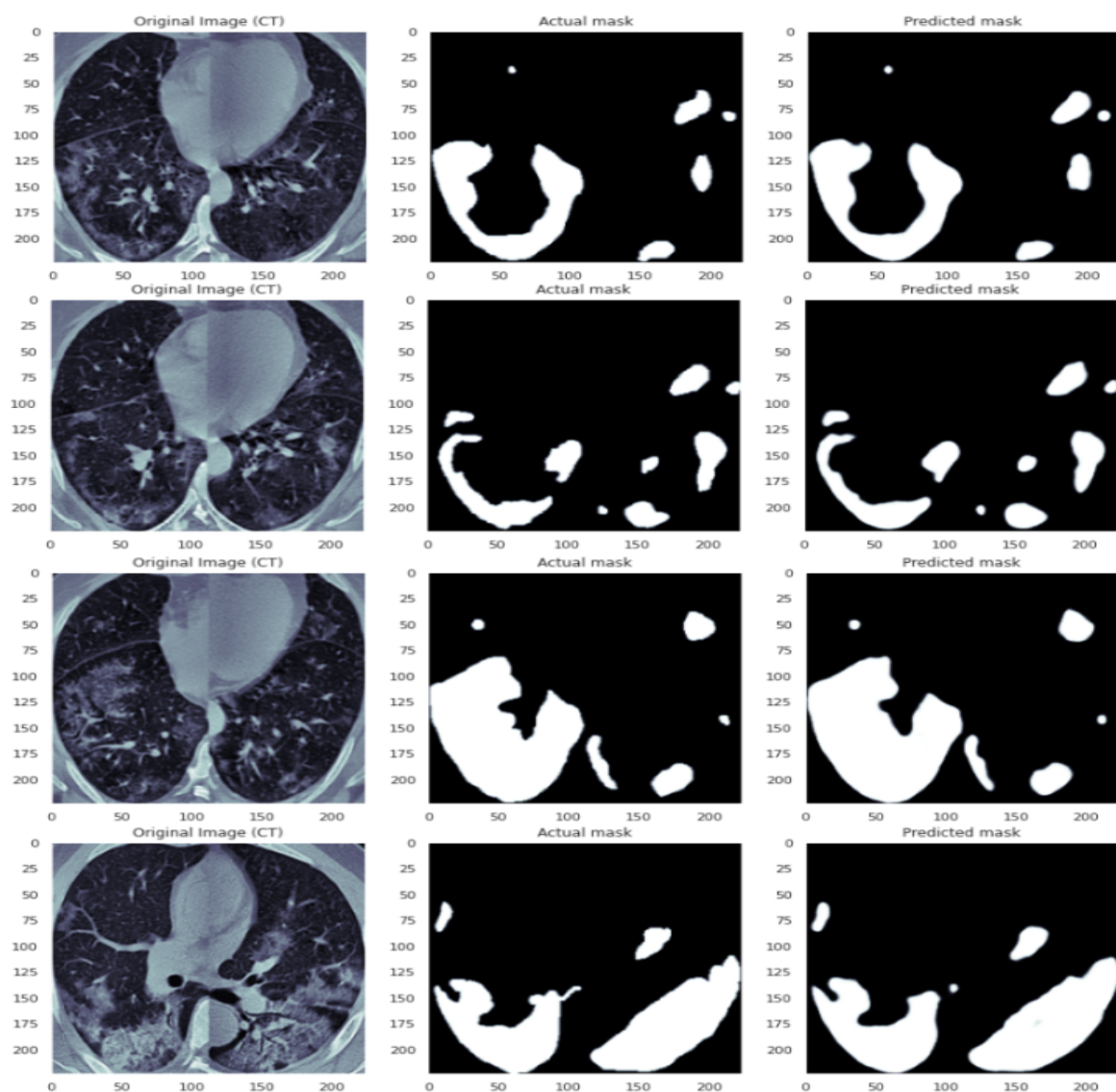


Figure 14. Visual qualitative comparison of the infection segmentation results between the ground truth and our proposed model on four slices from different CT scans. First column: original CT scan. Second column: ground truth. Third column: predicted infection masks.

5. Discussion

As previously mentioned, many deep learning algorithms have been used for the diagnosis of COVID-19 complications using CT or X ray images and they have achieved good classification performances; however, most of the results are obtained without knowledge of clinical characteristics of COVID-19. Moreover, the results analysis is only reported as metric values such as accuracy and AUC, without showing a clinical image that could be validated by radiologists. The aforementioned limitations constrain the translation of deep learning model into clinical practice. In this study, we proposed a new a 3D visualization of COVID-19 complications, which facilitate their interpretation by radiologists. An accurate training model requires sufficient annotated medical imaging data. On the other hand, high quantities of information from multiple sources are likely to overfit training and to lose the main clinical features. Not to mention that the collected data is heavily influenced by the instructions provided to the annotators. For this reason, the proposed framework achieved good performances for the different system's components, and at the same time, dealt with the reduced dataset used for training.

For further evaluation, we quantitatively compared the performance of the proposed lungs and infection segmentation models with other state of the art methods that used the same publicly available dataset we used for training and testing, which renders the comparison to be interesting. We considered the works of Ma et al. [41] who proposed a U-net based deep learning system, Muller et al. [47], where a standard 3D U-Net architecture was implemented, Omar Alirr [48], where two cascaded deep FCNs are connected sequentially to segment the lung organ and then the COVID-19 infection areas with an adjustment of U-net architecture as a backbone, and Punn et Agarwal [49], who developed their network with a two cascaded residual attention inception U-Net (RAIU-Net) model to generate lung contour maps and COVID-19 infected regions. Quantitative results, using the dice coefficient metric as a reference and including lungs and infection segmentation models, are reported in Table 6 below.

Table 6. Quantitative comparison of COVID-19 CT lung and infection segmentation results in terms of Dice Coefficient.

Works	Lungs Segmentation	Infection Segmentation
Ma et al. [38]	0.977	0.673
Muller et al. [44]	0.956	0.761
Omar Alirr [45]	0.961	0.780
Punn et Agarwal [46]	0.96	0.81
Proposed method	0.98	0.91

The results prove the effectiveness of our models that outperformed the other listed methods by achieving the highest Dice Coefficient value for both lungs and infection segmentation models.

6. Conclusions

In this study, the development and deployment of a deep learning-based diagnosis system to assist novel coronavirus pneumonia screening using CT imaging is proposed. The segmentation subsystem, developed using the popular U-Net architecture as the main framework, will highlight the position of the infected areas, whereas the classification subsystem and the semi-automated 3D reconstruction subsystem will give an idea about the probability of being infected with the virus, along with the infection rate in case of positive findings. The quantitative and qualitative evaluation results demonstrated the effectiveness of our system in accurately localizing and quantifying the infection regions from CT scans. It also showed that the developed models outperform the other recently proposed approaches which were evaluated using standard benchmark performance metrics such as the dice score, for which we achieved 0.98 and 0.91 for the lung and infection segmentation tasks, respectively, and the accuracy, for which we achieved 0.98 for the classification task. The main limitation of this study is the use of a small, but sufficient number, of model training data. Confidentiality restrictions and the high cost of labeling partly explain the absence of a large number of COVID-19 clinical CT images. Indeed, combining datasets collected under different labeling regimes is often problematic because, in general, the data collected is heavily influenced by the instructions provided to annotators. For this reason, a workflow aimed at obtaining good performances for the different systems' components, while at the same time, dealing with reduced datasets used for training, is proposed. For future work, we intend to fully automate the volume reconstruction module to enable a real time 3D screening result.

Author Contributions: Conceptualization, R.M. (Ramzi Mahmoudi); methodology, R.M. (Ramzi Mahmoudi) and N.B.; software, R.M. (Rania Mabrouk); formal analysis, M.A.M. and B.G.-Z.; writing—original draft preparation, R.M. (Ramzi Mahmoudi) and N.B.; writing—review and editing, M.H.B. All authors have read and agreed to the published version of the manuscript.

Funding: This work was supported by The Francophone University Agency (AUF) COVID-19.1 PANDEMIC SPECIAL PLAN. Project ID 469, Title: Development and implementation of a decision support system based on artificial intelligence applied to medical imaging to improve the management of patients with SARS-CoV2 (SPECTRUM) (2020).

Institutional Review Board Statement: Not applicable.

Informed Consent Statement: Not applicable.

Data Availability Statement: The data that support the findings of this study are available from the lung CTS dataset of Ma Jun et al. Further details can be found at: <https://coronacases.org/> (accessed on 15 December 2021) and <https://radiopaedia.org/> (accessed on 15 December 2021).

Conflicts of Interest: The authors declare no conflict of interest.

References

1. Wang, C.; Horby, P.W.; Hayden, F.G.; Gao, G.F. A novel coronavirus outbreak of global health concern. *Lancet* **2020**, *395*, 470–473. [[CrossRef](#)]
2. Wang, W.; Xu, Y.; Gao, R.; Lu, R.; Han, K.; Wu, G.; Tan, W. Detection of SARS-CoV-2 in Different Types of Clinical Specimens. *JAMA* **2020**, *323*, 1843–1844. [[CrossRef](#)] [[PubMed](#)]
3. World Health Organization. WHO Director-General's Opening Remarks at the Media Briefing on COVID-19. 2020. Available online: <https://www.who.int/director-general/speeches/detail/who-director-general-s-opening-remarks-at-the-media-briefing-on-covid-19> (accessed on 11 March 2020).
4. World Health Organization. WHO Coronavirus (COVID-19) Dashboard. WHO (COVID-19) Homepage. Available online: <https://covid19.who.int/table> (accessed on 1 May 2022).
5. Benameur, N.; Mahmoudi, R.; Zaid, S.; Arous, Y.; Hmida, B.; Bedoui, M.H. SARS-CoV-2 diagnosis using medical imaging techniques and artificial intelligence: A review. *Clin. Imaging* **2021**, *76*, 6–14. [[CrossRef](#)] [[PubMed](#)]
6. World Health Organization. Statement on the Second Meeting of the International Health Regulations. 2005. Available online: [https://www.who.int/news/item/30-01-2020-statement-on-the-second-meeting-of-the-international-health-regulations-\(2005\)-emergency-committee-regarding-the-outbreak-of-novel-coronavirus-\(2019-ncov\)](https://www.who.int/news/item/30-01-2020-statement-on-the-second-meeting-of-the-international-health-regulations-(2005)-emergency-committee-regarding-the-outbreak-of-novel-coronavirus-(2019-ncov) (accessed on 1 May 2022).
7. Tingbo, L.; Yu, L. Handbook of COVID-19 Prevention and Treatment. Tools, Guidelines and Methodologies. 2020. Available online: <https://covid-19.alibabacloud.com/> (accessed on 15 December 2021).
8. Fang, Y.; Zhang, H.; Xie, J.; Lin, M.; Ying, L.; Pang, P.; Ji, W. Sensitivity of Chest CT for COVID-19: Comparison to RT-PCR. *Radiology* **2020**, *296*, 20200432. [[CrossRef](#)] [[PubMed](#)]
9. Ai, T.; Yang, Z.; Hou, H.; Zhan, C.; Chen, C.; Lv, W.; Tao, Q.; Sun, Z.; Xia, L. Correlation of Chest CT and RT-PCR Testing for Coronavirus Disease 2019 (COVID-19) in China: A Report of 1014 Cases. *Radiology* **2020**, *296*, E32–E40. [[CrossRef](#)] [[PubMed](#)]
10. Dong, D.; Tang, Z.; Wang, S.; Hui, H.; Gong, L.; Lu, Y.; Xue, J.; Liao, H.; Chen, F.; Yang, F.; et al. The Role of Imaging in the Detection and Management of COVID-19: A Review. *IEEE Rev. Biomed. Eng.* **2020**, *14*, 16–29. [[CrossRef](#)]
11. Bernheim, A.; Mei, X.; Huang, M.; Yang, Y.; Fayad, Z.A.; Zhang, N.; Diao, K.; Lin, B.; Zhu, X.; Li, K.; et al. Chest CT Findings in Coronavirus Disease-19 (COVID-19): Relationship to Duration of Infection. *Radiology* **2020**, *295*, 200463. [[CrossRef](#)]
12. E Kaufman, A.; Naidu, S.; Ramachandran, S.; Kaufman, D.S.; A Fayad, Z.; Mani, V. Review of radiographic findings in COVID-19. *World J. Radiol.* **2020**, *12*, 142–155. [[CrossRef](#)]
13. Litjens, G.; Kooi, T.; Bejnordi, B.E.; Setio, A.A.A.; Ciompi, F.; Ghafoorian, M.; van der Laak, J.A.W.M.; van Ginneken, B.; Sánchez, C.I. A survey on deep learning in medical image analysis. *Med. Image Anal.* **2017**, *42*, 60–88. [[CrossRef](#)]
14. Hu, Z.; Tang, J.; Wang, Z.; Zhang, K.; Zhang, L.; Sun, Q. Deep learning for image-based cancer detection and diagnosis—A survey. *Pattern Recognit.* **2018**, *83*, 134–149. [[CrossRef](#)]
15. Voulodimos, A.; Doula, N.; Doula, A.; Protopapadakis, E. Deep Learning for Computer Vision: A Brief Review. *Comput. Intell. Neurosci.* **2018**, *2018*, 7068349. [[CrossRef](#)] [[PubMed](#)]
16. Shi, F.; Wang, J.; Shi, J.; Wu, Z.; Wang, Q.; Tang, Z.; He, K.; Shi, Y.; Shen, D. Review of Artificial Intelligence Techniques in Imaging Data Acquisition, Segmentation, and Diagnosis for COVID-19. *IEEE Rev. Biomed. Eng.* **2020**, *14*, 4–15. [[CrossRef](#)] [[PubMed](#)]
17. Wang, L.; Lin, Z.Q.; Wong, A. COVID-Net: A tailored deep convolutional neural network design for detection of COVID-19 cases from chest X-ray images. *Sci. Rep.* **2020**, *10*, 19549. [[CrossRef](#)] [[PubMed](#)]
18. ElAraby, M.E.; Elzeki, O.M.; Shams, M.Y.; Mahmoud, A.; Salem, H. A novel Gray-Scale spatial exploitation learning Net for COVID-19 by crawling Internet resources. *Biomed. Signal Process. Control* **2021**, *73*, 103441. [[CrossRef](#)]
19. Ahuja, S.; Panigrahi, B.K.; Dey, N.; Rajinikanth, V.; Gandhi, T.K. Deep transfer learning-based automated detection of COVID-19 from lung CT scan slices. *Appl. Intell.* **2020**, *51*, 571–585. [[CrossRef](#)]
20. Fan, D.-P.; Zhou, T.; Ji, G.-P.; Zhou, Y.; Chen, G.; Fu, H.; Shen, J.; Shao, L. Inf-Net: Automatic COVID-19 Lung Infection Segmentation from CT Images. *IEEE Trans. Med. Imaging* **2020**, *39*, 2626–2637. [[CrossRef](#)]
21. Shan, F.; Gao, Y.; Wang, J.; Shi, W.; Shi, N.; Han, M.; Xue, Z.; Shen, D.; Shi, Y. Lung Infection Quantification of COVID-19 in CT Images with Deep Learning. *arXiv* **2020**, arXiv:2003.04655.

22. Elzeki, O.M.; Elfattah, M.A.; Salem, H.; Hassanien, A.E.; Shams, M. A novel perceptual two layer image fusion using deep learning for imbalanced COVID-19 dataset. *PeerJ Comput. Sci.* **2021**, *7*, e364. [[CrossRef](#)]
23. Wu, Y.-H.; Gao, S.-H.; Mei, J.; Xu, J.; Fan, D.-P.; Zhang, R.-G.; Cheng, M.-M. JCS: An Explainable COVID-19 Diagnosis System by Joint Classification and Segmentation. *IEEE Trans. Image Process.* **2021**, *30*, 3113–3126. [[CrossRef](#)]
24. Gozes, O.; Frid-Adar, M.; Greenspan, H.; Browning, P.D.; Zhang, H.; Ji, W.; Bernheim, A.; Siegel, E. Rapid AI Development Cycle for the Coronavirus (COVID-19) Pandemic: Initial Results for Automated Detection & Patient Monitoring Using Deep Learning CT Image Analysis. *arXiv* **2020**, arXiv:2003.05037.
25. Milletari, F.; Navab, N.; Ahmadi, S.-A. V-net: Fully convolutional neural networks for volumetric medical image segmentation. In Proceedings of the 2016 Fourth International Conference on 3D Vision (3DV), Stanford, CA, USA, 25–28 October 2016; pp. 565–571.
26. Gao, S.-H.; Cheng, M.-M.; Zhao, K.; Zhang, X.-Y.; Yang, M.-H.; Torr, P.H. Res2Net: A New Multi-Scale Backbone Architecture. *IEEE Trans. Pattern Anal. Mach. Intell.* **2019**, *43*, 652–662. [[CrossRef](#)] [[PubMed](#)]
27. Simonyan, K.; Zisserman, A. Very Deep Convolutional Networks for Large-Scale Image Recognition. *arXiv* **2015**, arXiv:1409.1556.
28. He, K.; Zhang, X.; Ren, S.; Sun, J. Deep residual learning for image recognition. In Proceedings of the 2016 IEEE Conference on Computer Vision and Pattern Recognition (CVPR), Las Vegas, NV, USA, 27–30 June 2016; pp. 770–778. [[CrossRef](#)]
29. Selvaraju, R.R.; Cogswell, M.; Das, A.; Vedantam, R.; Parikh, D.; Batra, D. Grad-CAM: Visual Explanations from Deep Networks via Gradient-Based Localization. In Proceedings of the 2017 IEEE International Conference on Computer Vision (ICCV), Venice, Italy, 22–29 October 2017; pp. 618–626. [[CrossRef](#)]
30. Yamashita, R.; Nishio, M.; Do, R.K.G.; Togashi, K. Convolutional neural networks: An overview and application in radiology. *Insights Imaging* **2018**, *9*, 611–629. [[CrossRef](#)] [[PubMed](#)]
31. Ankile, L.L.; Heggland, M.F.; Krange, K. Deep Convolutional Neural Networks: A survey of the Foundations, Selected Improvements, and Some Current Applications. *arXiv* **2020**, arXiv:2011.12960.
32. Gu, J.; Wang, Z.; Kuen, J.; Ma, L.; Shahroudy, A.; Shuai, B.; Liu, T.; Wang, X.; Wang, G.; Cai, J.; et al. Recent advances in convolutional neural networks. *arXiv* **2015**, arXiv:1512.07108. [[CrossRef](#)]
33. Khan, A.; Sohail, A.; Zahoor, U.; Qureshi, A.S. A survey of the recent architectures of deep convolutional neural networks. *Artif. Intell. Rev.* **2020**, *53*, 5455–5516. [[CrossRef](#)]
34. Shelhamer, E.; Long, J.; Darrell, T. Fully Convolutional Networks for Semantic Segmentation. *arXiv* **2015**, arXiv:1411.4038. [[CrossRef](#)]
35. Ronneberger, O.; Fischer, P.; Brox, T. U-Net: Convolutional Networks for Biomedical Image Segmentation. *arXiv* **2015**, arXiv:1505.04597.
36. Iglovikov, V.; Mushinskiy, S.; Osin, V. Satellite Imagery Feature Detection Using Deep Convolutional Neural Network: A Kaggle Competition. *arXiv* **2017**, arXiv:1706.06169.
37. Iglovikov, V.; Shvets, A. TernausNet: U-Net with VGG11 Encoder Pre-Trained on ImageNet for Image Segmentation. *arXiv* **2018**, arXiv:1801.05746.
38. Ma, J.; Ge, C.; Wang, Y.; An, X.; Gao, J.; Yu, Z.; Zhang, M.; Liu, X.; Deng, X.; Cao, S. COVID-19 CT Lung and Infection Segmentation Dataset. *Zenodo* **2020**, *20*. [[CrossRef](#)]
39. RAISS.com. Coronacases. Available online: <https://coronacases.org/> (accessed on 1 May 2022).
40. Radiopaedia Pty Ltd. ACN 133 562 722. Available online: <https://radiopaedia.org/> (accessed on 1 May 2022).
41. Ma, J.; Wang, Y.; An, X.; Ge, C.; Yu, Z.; Chen, J.; Zhu, Q.; Dong, G.; He, J.; He, Z.; et al. Towards Data-Efficient Learning: A Benchmark for COVID-19 CT Lung and Infection Segmentation. *arXiv* **2020**, arXiv:2004.12537. [[CrossRef](#)] [[PubMed](#)]
42. Pizer, S.M.; Amburn, E.P.; Austin, J.D.; Cromartie, R.; Geselowitz, A.; Greer, T.; ter Haar Romeny, B.; Zimmerman, J.B.; Zuiderveld, K. Adaptive histogram equalization and its variations. *Comput. Vis. Graph. Image Process.* **1987**, *39*, 355–368. [[CrossRef](#)]
43. Zimmerman, J.; Pizer, S.; Staab, E.; Perry, J.; McCartney, W.; Brenton, B. An evaluation of the effectiveness of adaptive histogram equalization for contrast enhancement. *IEEE Trans. Med. Imaging* **1988**, *7*, 304–312. [[CrossRef](#)]
44. Pizer, S.; Johnston, R.; Erickson, J.; Yankaskas, B.; Muller, K. Contrast-limited adaptive histogram equalization: Speed and effectiveness. In Proceedings of the First Conference on Visualization in Biomedical Computing, Atlanta, GA, USA, 22–25 May 1990; pp. 337–345. [[CrossRef](#)]
45. Hussain, Z.; Gimenez, F.; Yi, D.; Rubin, D. Differential Data Augmentation Techniques for Medical Imaging Classification Tasks. *AMIA Annu. Symp. Proc.* **2017**, *2017*, 979–984.
46. ThermoFisher. AMIRA Software. Available online: <https://www.thermofisher.com/tm/en/home/electron-microscopy/products/software-em-3d-vis/amira-software.html> (accessed on 15 December 2021).
47. Müller, D.; Rey, I.S.; Kramer, F. Automated Chest CT Image Segmentation of COVID-19 Lung Infection based on 3D U-Net. *arXiv* **2020**, arXiv:2007.04774.
48. Alirr, O.I. Automatic Deep Learning System for COVID-19 Infection Quantification in Chest CT. Available online: <https://arxiv.org/ftp/arxiv/papers/2010/2010.01982.pdf> (accessed on 15 December 2021).
49. Punn, N.S.; Agarwal, S. CHS-Net: A Deep Learning Approach for Hierarchical Segmentation of COVID-19 Infected CT Images. *arXiv* **2021**, arXiv:2012.07079. [[CrossRef](#)]